PAPER

Phase-field modeling of nanostructural evolution in physical vapor deposited phase-separating ternary alloy films

To cite this article: Rahul Raghavan et al 2022 Modelling Simul. Mater. Sci. Eng. 30 084004

View the article online for updates and enhancements.

You may also like

- Time-Resolved Nanostructural Analysis of Thin-Film Formation Process from Nafion Solution by Synchrotron X-Ray Scattering Yuichi Konosu, Hiroyasu Masunaga, Takaaki Hikima et al.
- SAXS-CT: a nanostructure resolving microscopy for macroscopic biologic specimens

A L C Conceição, J Perlich, S Haas et al.

- Effect of Au film mask on antiwetting and antireflection properties of nanostructural polymer by plasma nanotexturing Xiao-Yu Li, Yu-Peng Li, Lei Huo et al.



IOP ebooks™

Bringing together innovative digital publishing with leading authors from the global scientific community.

Start exploring the collection-download the first chapter of every title for free.

Phase-field modeling of nanostructural evolution in physical vapor deposited phase-separating ternary alloy films

Rahul Raghavan, Peichen Wu and Kumar Ankit*

Materials Science & Engineering, School for Engineering of Matter, Transport and Energy, Arizona State University, 551 E. Tyler Mall, Tempe, AZ 85287-6106, United States of America

E-mail: kumar.ankit@asu.edu

Received 1 June 2022; revised 17 October 2022 Accepted for publication 4 November 2022 Published 14 November 2022



Abstract

Self-assembly by spinodal decomposition is known to be a viable route for synthesizing nanoscaled interfaces in a variety of materials, including metamaterials. In order to tune the response of these specialized materials to external stimuli, knowledge of processing-nanostructure correlations is required. Such an understanding is more challenging to obtain purely by experimental means due to complexity of multicomponent atomic diffusion mechanisms that govern the nanostructural self-assembly. In this work, we introduce a phase-field modeling approach which is capable of simulating the nanostructural evolution in ternary alloy films that are typically synthesized using physical vapor deposition. Based on an extensive parametric study, we analyze the role of the deposition rate and alloy composition on the nanostructural self-assembly in ternary alloy films. The simulated nanostructures are categorized on the basis of nanostructured morphology and mapped over a compositional space to correlate the processing conditions with the film nanostructures. The morphology maps reveal that while deposition rate governs the nanostructural evolution at around equi-molar compositions, the impact of composition on nanostructuring is more pronounced when the atomic ratios of alloying elements are skewed.

Keywords: phase-field model, ternary alloys, phase separation, PVD, diffusion-controlled

(Some figures may appear in colour only in the online journal)

1361-651X/22/084004+16\$33.00 © 2022 IOP Publishing Ltd Printed in the UK

^{*} Author to whom any correspondence should be addressed.

1. Introduction

Metamaterials are described as engineered periodic composites for altering electromagnetic properties of materials to obtain responses that are not observed naturally. The presence of nanoscale modulations or periodicities allows for tuning of these responses e.g. in optical metamaterials, where the periodicity of nanostructures allows them to operate in the visible and near-infrared wavelength regimes, that induce negative refraction, optical magnetism, and hyperbolic dispersion. For fabricating 3D metamaterials, techniques such as multilayer deposition, nano-imprinting, and layer-by-layer lithography can be employed. However, apart from materials and process control challenges, these techniques induce roughness at interfaces which contributes to scattering loss. Bottom-up techniques that leverage nanoscale phase separation, such as electrochemically grown metal wire arrays, block copolymer self-assembly, DNA-assisted self-assembly of nanoparticles, and pulsed-laser deposition, are useful alternatives for synthesizing metamaterials, however, most of these approaches require labor- and time-intensive post-processing steps.

Self-assembly via spinodal decomposition is known to be a viable route for synthesizing nanoscaled interfaces in metamaterials [1–4]. In the context of thin films, fabrication is typically accomplished by sputtering two or more pure elements on a substrate; depending on processing conditions, ensuing phase separation results in nanostructured interfaces that are characterized by lateral, vertical, or random concentration modulations. The development of films with periodic nanoscale patterns has been the focus of considerable research due to a variety of applications, including in optoelectronics, superconductivity, and catalysis [5–8]. Tuning the morphology of nanostructured interfaces in these materials requires the knowledge of processing-nanostructure relations that are non-trivial to establish, particularly due to complex multicomponent atomic diffusion mechanisms that govern the nanostructural self-assembly.

Numerous studies have explored nanoscale morphologies in phase-separated binary alloy films. As mentioned above, two-phase films with near-equal atomic percentages of the alloying components have yielded vertical concentration modulations (VCMs) where the two phases form layered domains [9–13], lateral concentration modulations (LCMs) where the phases separate into interpenetrating shafts that grow vertically [14–19], and mixed morphologies with characteristics of both LCMs and VCMs [20–22]. When the elemental film compositions deviate slightly from equiatomic, additional variants, namely, aligned rods, and perforated VCMs evolve. While the former comprises rods of the minority phase that grow vertically in a matrix of the majority phase [22–24], the latter consists of continuous layered domains alternating with a bicontinuous network of the majority and minority phases that are stacked perpendicular to the deposition axis. However, when the elemental composition ratio is highly skewed, globules of the minority phase within the matrix of the majority phase evolve [22].

Previous investigations on morphological evolution in *ternary* phase-separating systems have primarily focused on bulk multicomponent alloys [25–27] and rapidly cooled bulk metallic glasses [28–30]. However, a comprehensive study of phase separation during the synthesis of ternary vapor-deposited films has never before been done. Self-assembled morphologies such as those demonstrated in binary alloys are likely to form in ternary immiscible alloy films, as well, however, the state-of-the-art phase-field modeling studies are limited to binary alloys [20–22]. Since actual physical vapor deposition (PVD) experiments and characterization of nanostructured domains formed using high-resolution electron microscopy is resource-intensive, a numerical modeling technique that is capable of simulating the nanostructural evolution in films for a range of compositions, temperatures, and deposition rates can render deeper insights into the phase separation mechanisms. With this objective, in the following study, we reformulate a previous-reported ternary phase-field model by Chen [31]

and Bhattacharyya *et al* [32] to mimic the PVD process. The primary goal is to predict the morphological evolution during co-deposition of phase-separating ternary alloy films for an entire range of compositions and deposition conditions. Based on our simulations, we report a rich variety of previously unknown periodic morphologies such as pseudo-VCM (pV), coreshell (CS), binary, and ternary LCMs. Finally, we classify the characteristic morphologies by constructing morphology maps.

2. Phase-field model

In this section, we revisit a phase-field model based on a ternary Cahn–Hilliard approach to simulate the nanostructural evolution in ternary phase separating alloy films with reference elemental components A, B, and C [31, 33, 34]. Phase separation occurs via the minimization of the total free energy functional which is given by

$$F = \int_{V} N_{\upsilon} \left[f(\phi_{A}, \phi_{B}, \phi_{C}) + \kappa_{A} (\nabla \phi_{A})^{2} + \kappa_{B} (\nabla \phi_{B})^{2} + \kappa_{C} (\nabla \phi_{C})^{2} \right] dV, \tag{1}$$

where, N_{v} represents the number of molecules per unit volume and is assumed to be independent of composition and space, while κ_{i} (i = A, B, and C) are the gradient parameters associated with the concentration fields. The order parameters, ϕ_{A} , ϕ_{B} , and ϕ_{C} denote the scaled concentrations of the alloying elements, A, B, and C in the film, such that their sum equals unity to conserve mass

$$\phi_{\mathbf{A}} + \phi_{\mathbf{B}} + \phi_{\mathbf{C}} = 1. \tag{2}$$

The chemical free energy per molecule, $f(\phi_A, \phi_B, \phi_C)$, follows a regular solution model, such that

$$\frac{1}{k_{\rm B}T}f(\phi_{\rm A},\phi_{\rm B},\phi_{\rm C}) = \sum_{i\neq j}\chi_{ij}\phi_i\phi_j + \sum_i\phi_i\log\phi_i,\tag{3}$$

where, χ_{ij} (i,j=A,B,v; $i\neq j$) are the pairwise interaction coefficients between the components, k_B is the Boltzmann constant, and T, the absolute temperature. Equation (3) can be expanded and re-written as

$$f(\phi_{A}, \phi_{B}, \phi_{C}) = k_{B}T[\chi_{AB}\phi_{A}\phi_{B} + \chi_{B\upsilon}\phi_{B}\phi_{C} + \chi_{A\upsilon}\phi_{A}\phi_{C} + \phi_{A}\log\phi_{A} + \phi_{B}\log\phi_{B} + \phi_{C}\log\phi_{C}].$$

$$(4)$$

 $\phi_{\rm C}$ can be eliminated by replacing with $(1-\phi_{\rm A}-\phi_{\rm B})$ in equation (4), and rewriting as

$$f(\phi_{A}, \phi_{B}) = k_{B}T[\chi_{AB}\phi_{A}\phi_{B} + \chi_{B\nu}\phi_{B}(1 - \phi_{A} - \phi_{B}) + \chi_{A\nu}\phi_{A}(1 - \phi_{A} - \phi_{B}) + \phi_{A}\log\phi_{A} + \phi_{B}\log\phi_{B} + (1 - \phi_{A} - \phi_{B})\log(1 - \phi_{A} - \phi_{B})].$$
 (5)

The chemical potentials, μ_A and μ_B , corresponding to the A-rich α and B-rich β phases are obtained by performing the variational derivatives of the free energy functional in equation (1) with respect to ϕ_A and ϕ_B , such that

$$\mu_{\rm A} = \frac{\delta F}{\delta \phi_{\rm A}} = \frac{\partial f}{\partial \phi_{\rm A}} - 2\kappa_{\rm AA} \nabla^2 \phi_{\rm A} - 2\kappa_{\rm AB} \nabla^2 \phi_{\rm B} \tag{6}$$

and

$$\mu_{\rm B} = \frac{\delta F}{\delta \phi_{\rm B}} = \frac{\partial f}{\partial \phi_{\rm B}} - 2\kappa_{\rm BB} \nabla^2 \phi_{\rm B} - 2\kappa_{\rm BA} \nabla^2 \phi_{\rm A},\tag{7}$$

where, $\kappa_{AA} = \kappa_A + \kappa_C$, $\kappa_{BB} = \kappa_B + \kappa_C$, and $\kappa_{AB} = \kappa_{BA} = \kappa_C$. We use a continuity equation to derive the phase-separation kinetics, which may be written as,

$$\frac{\partial \phi_i}{\partial t} = -\nabla \cdot J_i' \qquad i = A, B, C \tag{8}$$

where J_i is the net flux. We adopt a formulation that incorporates the net vacancy flux, J_o , during the diffusion process as reported earlier by Kramer *et al* [35, 36] and Bhattacharyya *et al* [32, 37], to obtain the net flux of each component, i, given by

$$J_i' = J_i + \phi_i J_\circ$$
 $i = A, B, C.$ (9)

Here, J_i is given by

$$J_i = -M_i \nabla \mu_i \qquad \qquad i = A, B, C \tag{10}$$

where, M_i and μ_i are the Onsager coefficient of the *i*th component and chemical potential per site, respectively. The vacancy flux, J_{\circ} , is given by

$$J_{\circ} = -(J_{\rm A} + J_{\rm B} + J_{\rm C}).$$
 (11)

By substituting equations (11) and (9) in equation (8) and using the Gibbs–Duhem relationship [36, 37], we obtain expressions for the temporal evolution of the α and β phases:

$$\frac{\partial \phi_{A}}{\partial t} = M_{AA} \nabla^{2} \left[\frac{\partial f}{\partial \phi_{A}} - 2\kappa_{AA} \nabla^{2} \phi_{A} - 2\kappa_{AB} \nabla^{2} \phi_{B} \right]
+ M_{AB} \nabla^{2} \left[\frac{\partial f}{\partial \phi_{B}} - 2\kappa_{BA} \nabla^{2} \phi_{A} - 2\kappa_{BB} \nabla^{2} \phi_{B} \right]$$
(12)

and

$$\frac{\partial \phi_{\rm B}}{\partial t} = M_{\rm BB} \nabla^2 \left[\frac{\partial f}{\partial \phi_{\rm B}} - 2\kappa_{\rm BB} \nabla^2 \phi_{\rm B} - 2\kappa_{\rm BA} \nabla^2 \phi_{\rm B} \right]
+ M_{\rm AB} \nabla^2 \left[\frac{\partial f}{\partial \phi_{\rm A}} - 2\kappa_{\rm AB} \nabla^2 \phi_{\rm B} - 2\kappa_{\rm AA} \nabla^2 \phi_{\rm A} \right],$$
(13)

where, M_{AA} and M_{BB} represent atomic mobilities of A and B atoms in non- α and non- β phases, respectively, while M_{AB} and M_{BA} represent mobilities of A atoms in β phase and B atoms in α phase, respectively [32, 36]. We extend the Nernst-Einstein relation to a ternary system [38] and couple the mobilities to the diffusion coefficients of the alloying components, D_i , using

$$M_{ii} = \frac{1}{k_{\rm B}T} D_i \phi_i (1 - \phi_i)$$
 $i, j = A, B, C$ (14)

and

$$M_{ij} = \frac{1}{k_{\rm B}T} D_i \phi_i \phi_j \qquad i, j = A, B, C \ i \neq j.$$
 (15)

We solve equations (12) and (13) by non-dimensionalizing the parameters using the characteristic length and time scales given by, $l^* = (\kappa_i/2k_BT)^{1/2}\Delta x$, and $t^* = (k_BT/M_{ii}^*l^{*2})$, respectively, where M_{ii}^* is the dimensional mobility for phase i = A, B. The equations (12) and (13) in

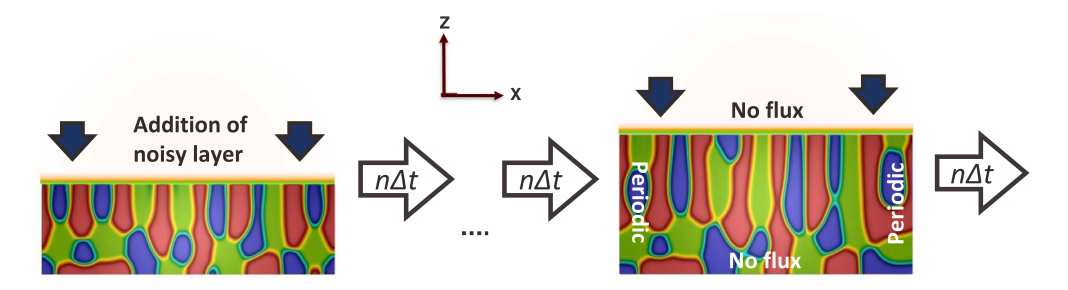


Figure 1. Schematic diagram illustrating a layer-by-layer deposition method adopted to simulate physical vapor deposition of ternary alloy films. The non-dimensional deposition rate, $\nu = 1/(n\Delta t)$, where Δt is the dimensionless time step for numerical integration and n is the number of time steps between the deposition of consecutive layers.

dimensionless form are solved via an explicit finite difference scheme for temporal and spatial derivatives. We follow a forward difference Euler scheme for the temporal derivatives and a second-order central difference for the spatial derivatives. The chemical potentials, μ_{II} and μ_{IJ} , I,J=A,B, $I\neq J$ are first calculated at each grid point. The discretized equations are given by

$$\mu_{II,i,j}^{t} = \left(\frac{\partial f}{\partial \phi_{I}}\right)_{i,j} - 2\kappa_{II} \frac{\phi_{I,i+1,j}^{t} + \phi_{I,i-1,j}^{t} + \phi_{I,i,j+1}^{t} + \phi_{I,i,j-1}^{t} - 4\phi_{I,i,j}^{t}}{h^{2}} - 2\kappa_{IJ} \frac{\phi_{J,i+1,j}^{t} + \phi_{J,i-1,j}^{t} + \phi_{J,i,j+1}^{t} + \phi_{J,i,j-1}^{t} - 4\phi_{J,i,j}^{t}}{h^{2}},$$
(16)

and

$$\mu_{IJ,i,j}^{t} = \left[\frac{\partial f}{\partial \phi_{J}}\right]_{i,j} - 2\kappa_{JI} \frac{\phi_{I,i+1,j}^{t} + \phi_{I,i-1,j}^{t} + \phi_{I,i,j+1}^{t} + \phi_{I,i,j-1}^{t} - 4\phi_{I,i,j}^{t}}{h^{2}} - 2\kappa_{JJ} \frac{\phi_{J,i+1,j}^{t} + \phi_{J,i-1,j}^{t} + \phi_{J,i,j+1}^{t} + \phi_{J,i,j-1}^{t} - 4\phi_{J,i,j}^{t}}{h^{2}}.$$
(17)

The Laplacian of the chemical potential is calculated by another central difference scheme such that the final equation in the discretized form reads

$$\frac{\partial \phi_{I}}{\partial t} = M_{II} \frac{\mu_{I,i+1,j}^{t} + \mu_{I,i-1,j}^{t} + \mu_{I,i,j+1}^{t} + \mu_{I,i,j-1}^{t} - 4\mu_{I,i,j}^{t}}{h^{2}} + M_{IJ} \frac{\mu_{IJ,i+1,j}^{t} + \mu_{IJ,i-1,j}^{t} + \mu_{IJ,i,j+1}^{t} + \mu_{IJ,i,j-1}^{t} - 4\mu_{IJ,i,j}^{t}}{h^{2}}.$$
(18)

A schematic diagram showing the computational technique for simulating nanostructural evolution in ternary films based on a temporally increasing box size is shown in figure 1. This two-dimensional simulation box consists of 300 grid points in the horizontal direction, while the film is grown in the vertical direction until the film thickness exceeds 300 grid points. The deposition is initialized from a seed layer of thickness $20\Delta z$ with average alloy composition, $\phi_{i,o} + \delta \phi_{i,o}$, (i = A,B,C), where $\delta \phi_{i,o}$ denotes the concentration fluctuation of $\approx \pm 0.05\%$. To simulate deposition flux and concurrent increase in film thickness, we add a fresh layer of a

 Table 1. Thermodynamic and kinetic parameters used for phase-field simulations.

Parameters	A	В	C	AB	AC	ВС
D	50	50	_	_	_	_
κ	4.0	4.0	4.0	_	_	
χ	_	_		3.5	3.5	3.5

noisy, non-decomposed mixture of the alloying components of thickness, Δz , at designated time intervals, $n\Delta t$, where n denotes the count of elapsed timesteps prior to addition of new layer. The non-dimensional deposition rate, ν , is given by $\frac{1}{n\Delta t}$. The relevant model parameters are listed in table 1. While periodic boundary conditions are imposed along the lateral edges of the film (x-axis), no-flux (Neumann) conditions are maintained along the deposition axis (z-axis). At this point, we caution that as opposed to actual PVD experiments, the deposition flux in the present phase-field model is assumed to be non-continuous with the lowest possible deposition rate being 1 grid point (Δz) per timestep (Δt). However, the above simulation approach has previously been reported to yield binary alloy film nanostructures that compare favorably with experiments [21, 22], therefore employing a similar approach to simulate nanostructural evolution in ternary films seems to be a reasonable choice. Based on the formulated model, we explore the influence of film composition and deposition rate on the evolution of characteristic nanoscale structures. We assign values ranging from 0.1 to 0.7 to ϕ_A , ϕ_B , and ϕ_C , ensuring that $\phi_A + \phi_B + \phi_C = 1$, and deposition rates, ν , that range from 0.31 $\leq \nu \leq 1.25$.

3. Characterization of self-assembled morphologies

In this section, we classify and analyze the distinct nanostructured morphologies that evolve when the film composition and deposition rate are varied. Depending on the morphology of the phase-separated domains, we categorize the resulting nanostructures into seven variants. As shown in figure 2, we map these variants on an isothermal section ($\chi=3.5$) of the phase diagram using the labels α , β , and γ , which correspond to A-rich, B-rich, and C-rich phases, respectively. Zone boundaries designate the regions across which nanostructural transitions are observed if the processing conditions are unaltered. We have also sub-divided the morphology map into inner, middle, and outer zones, which allows us to correlate the film nanostructure to the relative skew in the elemental composition.

3.1. Nanostructural evolution at inner zone compositions

The central or the inner zone consists of morphologies that form in the region where the composition of the alloying elements is nearly equal, i.e. in the range of 30–40 at.% X (X = A, B, C). Within the inner zone compositions, the A-rich, B-rich, and C-rich phases compete to form periodic nanostructures, giving rise to ternary lamellae at lower deposition rates, and vertically oriented beads and randomly phase-separated domains that show no self-organization, at larger deposition rates.

When the film composition is equimolar (33.33 at.%A, 33.33 at.%B, C), labeled P in figure 2, low deposition rates of $\nu \le 0.5$ results in the formation of vertically oriented ternary lamellae (tL), as shown in figure 3(a). Within the resulting nanocomposite, the three

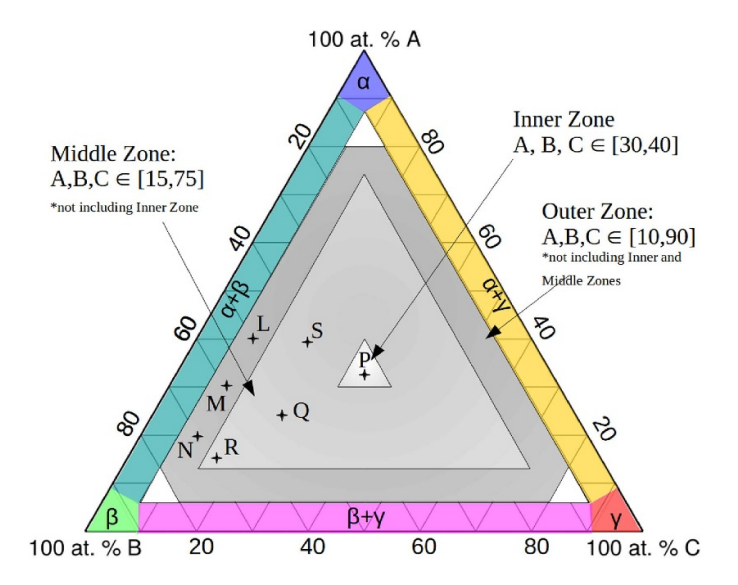


Figure 2. Compositional space divided into distinct zones, namely inner, middle, and outer. Labels in upper case pertain to compositions for which the corresponding nanostructural evolution has been discussed in the following sections of this manuscript.

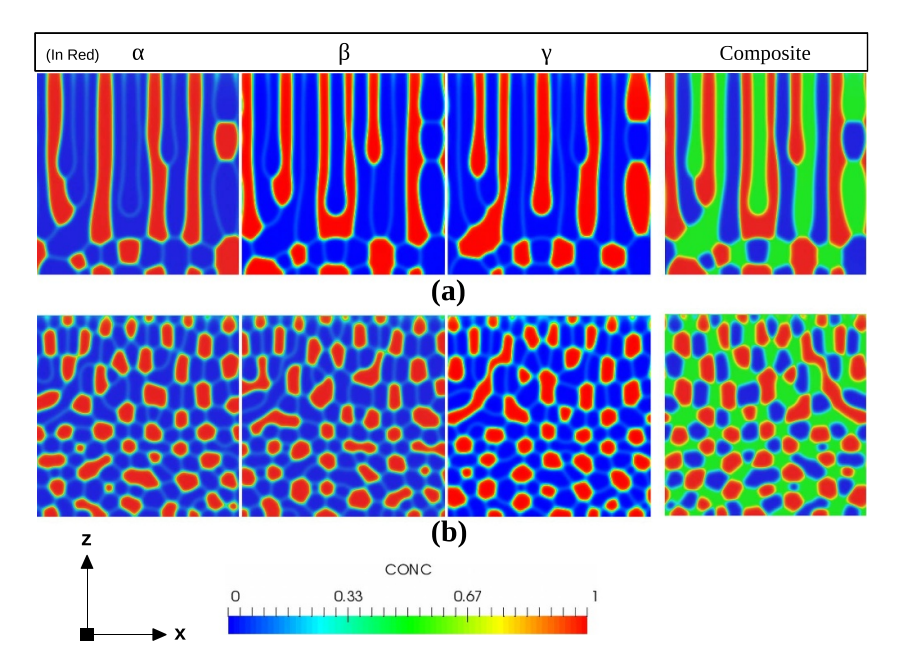


Figure 3. Nanostructural evolution of films at composition 33.33 *at.*%A, 33.33 *at.*%B, C forming (a) ternary lamellae (tL) at $\nu=0.5$ and (b) random non-assembled nanostructure (R) at $\nu=1.0$. α , β and γ phases are also plotted separately in red.

phase-separating domains form lamellae that are aligned parallel to the deposition axis but tri-continuous in the surface plane. A slow deposition rate combined with equal proportions of A, B, and C in the alloy film ensures that the phase separation is complete well before a fresh layer is added on top. Clearly, the penultimate layer i.e. the layer just below the film's surface acts as a template to drive successive phase separations in the newly deposited layer. The 'tL' nanostructure is also observed at other compositions, such as 30 at.%A, 30 at.%B, C, which falls within the inner zone, provided that the deposition rate is small enough such that phase separation kinetics exceeds the deposition rate. This is further accentuated by our parametric studies where tL film nanostructure stabilized when we varied the composition within the inner zone without altering the deposition rate. It can therefore be inferred that a slight deviation in the composition from equimolar does not impact the tL nanostructure.

Within the designated inner zone in figure 3(a), self-organization is lost at larger deposition rates ($\nu \geqslant 0.83$). Unlike the tLs that evolve at low deposition rates, random nanostructures with no apparent self-assembly, evolve when the deposition rate is increased. Figure 3(b) shows the α , β , and γ phases that do not self-assemble into a recognizable pattern. This absence of self-assembly arises from the larger ν , which ensures that no phase separation can occur on the film surface before a new layer is deposited. The normal vectors to the interfaces formed point in all possible directions, which indicates that the phase separation mechanism is similar to the one observed in the bulk nanostructure. Film depositions carried out at even higher rates for other composition variations within the inner zone, also produced similar random nanostructures.

3.2. Nanostructural evolution at middle zone compositions

Within the middle zone indicated in figure 2, at least one of the three elements, that comprise the alloy, always remains in minority, such that the atomic fraction of the minority element is below 0.33. Typically elemental compositions range from 15–75 at.% A and 15–75 at.% B whilst excluding any composition that falls within the inner zone. Film nanostructures that form in this region are diverse with interesting morphologies, such as vertically-oriented beads, and binary lamellae (bL) interspersed with globules, although the beaded morphologies dominate. Additionally, globular nanostructures that are relatively well-known are also observed to evolve.

At a film composition of 25 at.%A, 25 at.%B, C, shown in figure 2 as point Q, the minority α and β phases form alternating beads which align vertically in a γ matrix to form the vertically aligned bead morphology (B), as shown in figure 4(a). This type of self-assembly is favored for concentration ranges within the middle zone where one of the alloying elements forms a majority phase, while the remaining elements form minority phases of comparable atomic fractions. Beaded microstructures of ternary alloys undergoing spinodal decomposition have previously been reported [31, 32]. However, in the current simulations that correspond to film deposition, the nanostructured beads are observed to be aligned along the deposition axis, which in all certainty implies the impact of deposition kinetics on nanostructural evolution. Moreover, the beaded film nanostructures are found to be stable as we did not find these nanostructures to transition into any other morphology when simulations were repeated for several deposition rates.

At the film composition of 15 at.%A, 15 at.%B, C, labeled in figure 2 as R, A and B form α and β phases that separate out of the majority phase (C-rich, γ) while retaining a globular morphology. The initial separation occurs between the majority phase, γ , and an unseparated

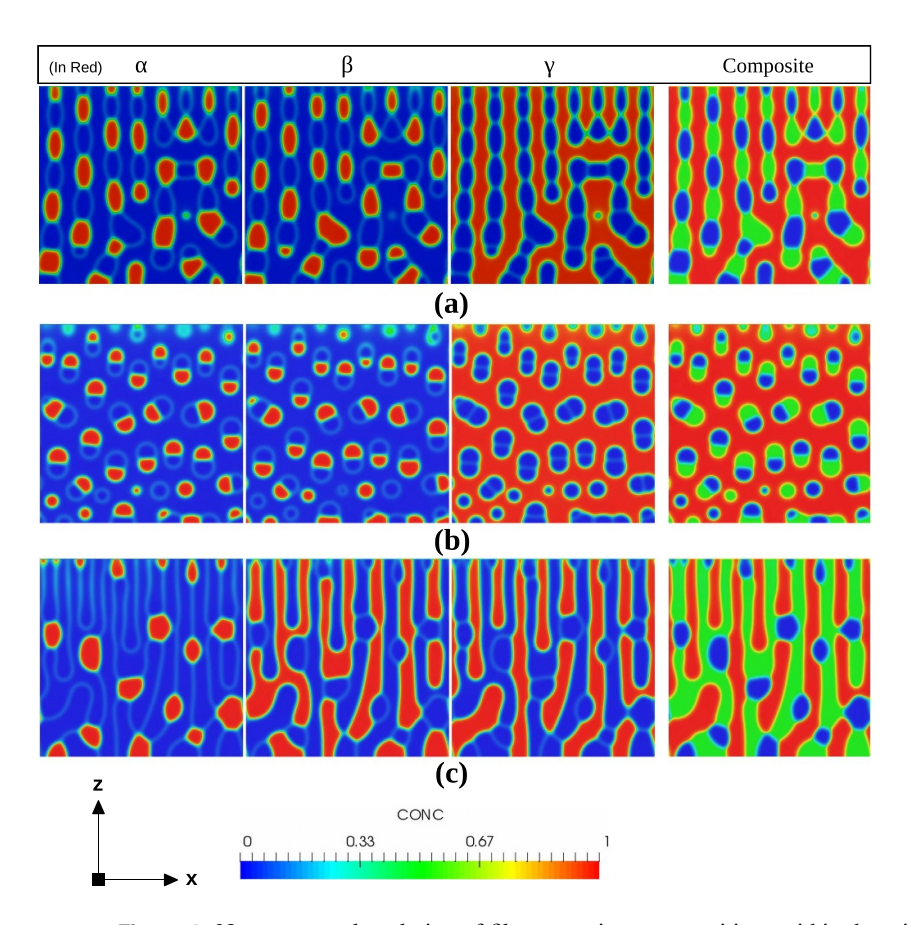


Figure 4. Nanostructural evolution of films at various compositions within the middle zone.(a) 25 *at.*%A, 25 *at.*%B, C resulting in vertically oriented beads (B), (b) 15 *at.*%A, 15 *at.*%B, C resulting in globular (G) morphology, and (c) 20 *at.*%A, 40 *at.*%B, C resulting in hybrid G-L morphology. Nanostructures show evolution of α , β and γ phases separately, as well as a composite.

transition phase, which then rapidly separates into jointed globules of α and β phases, as seen in figure 4(b). If the deposition rate is reduced ($\nu=0.31$ and 0.42), the joined globules undergo coarsening, as seen in figures 5(a) and (b). This is likely to happen at depositions performed at higher temperatures where atomic mobilities are larger. On the contrary, finer globules form at faster deposition rates ($\nu=0.83$ and 1.0). We also observed that the joined globules have a greater tendency to pinch off into independent globules at a faster deposition rate, as seen in figures 5(d) and (e). The globular morphology (G) is observed to evolve for a range of deposition rates for this composition, while at some of the other composition ratios, such as 20 at.%B, C, they transition to a beaded nanostructure for $\nu > 0.625$.

When the film composition is 20 at.%A, 40 at.%B, C (label S in figure 2), B and C form majority phases that evolve into vertical lamellae, while C forms a minority phase that evolves as globules dispersed amidst the lamellae, to form a hybrid G-L nanostructure, which is essentially a combination of bL (discussed above in section 3.3) and globules (G) (figure 4(c)).

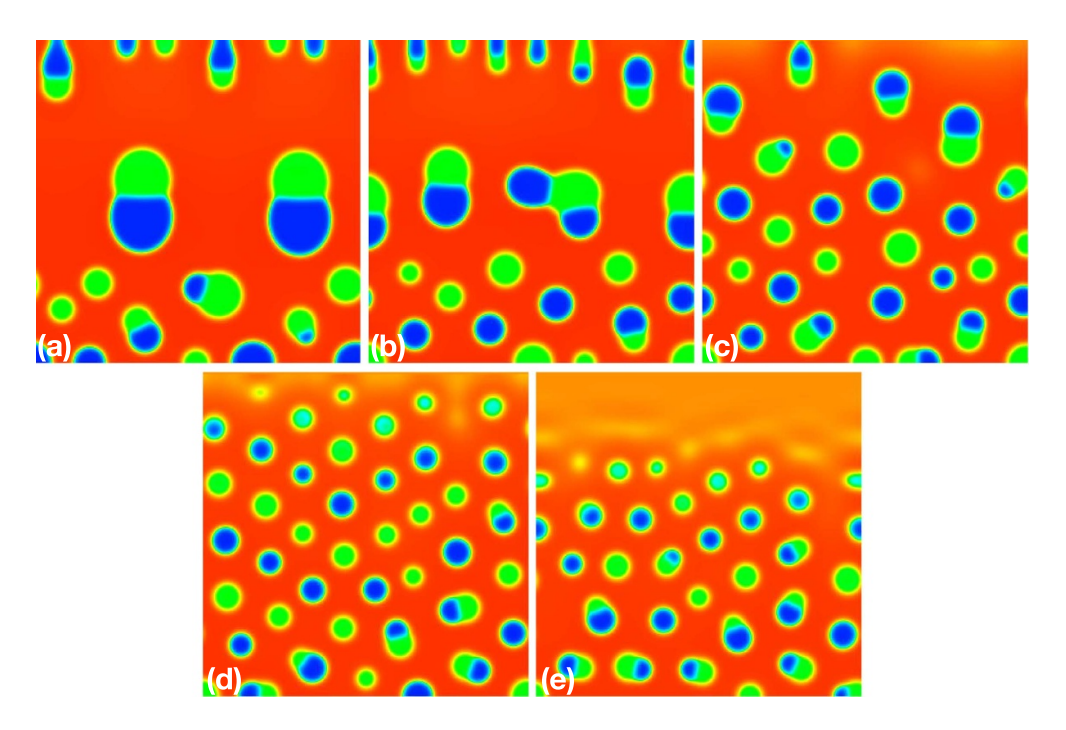


Figure 5. Figure morphological evolution of films of composition 15 at.% A 15 at.% B, C at non-dimensional deposition rates, ν , (a) 0.31 (b) 0.42 (c) 0.62 (d) 0.83 and (e) 1.0.

The G-L nanostructure, similar to the beaded and globular variants, was found to be stable for a wide range of deposition rates. The hybrid nanostructure is found to evolve all across the outer edge of the middle zone demarcated in figure 2, which is distinct from the LCM–VCM hybrids observed in binary phase-separated films [21].

3.3. Nanostructural evolution at outer zone compositions

As shown in figure 2, the outer zone has the largest disproportionality of alloying elements with the most concentrated element forming the majority phase, while the remaining two phases separate into minority phases. Moreover, when the composition of the third element is $\leq 10 \text{ at.}\%$ of the overall composition, it is unable to separate fully into a third phase leading to the formation of a metastable phase at the boundary between the majority and the minority phases. On the first glance, this nanostructure appears to be composed of two phases only, however, upon a closer examination, the metastable third phase at the interface can be observed.

At a film composition of 40 at.%A, 50 at.%B, C, indicated by point L in figure 2, a nanostructure that is primarily composed of α and β lamellae (bL) and resembles the LCM in binary immiscible alloy films [20–22], forms. As observed in figure 6(a), C does not fully separate into a stable γ phase, instead, it forms a metastable phase at the interface between α and β . Apparently, the formation of a nearly two phase nanostructure is caused due to a very low concentration of the third element. Unlike the tL and LCM morphologies which disappear when the deposition rate increases, the bL self-assembled nanostructures remain stable at all ν .

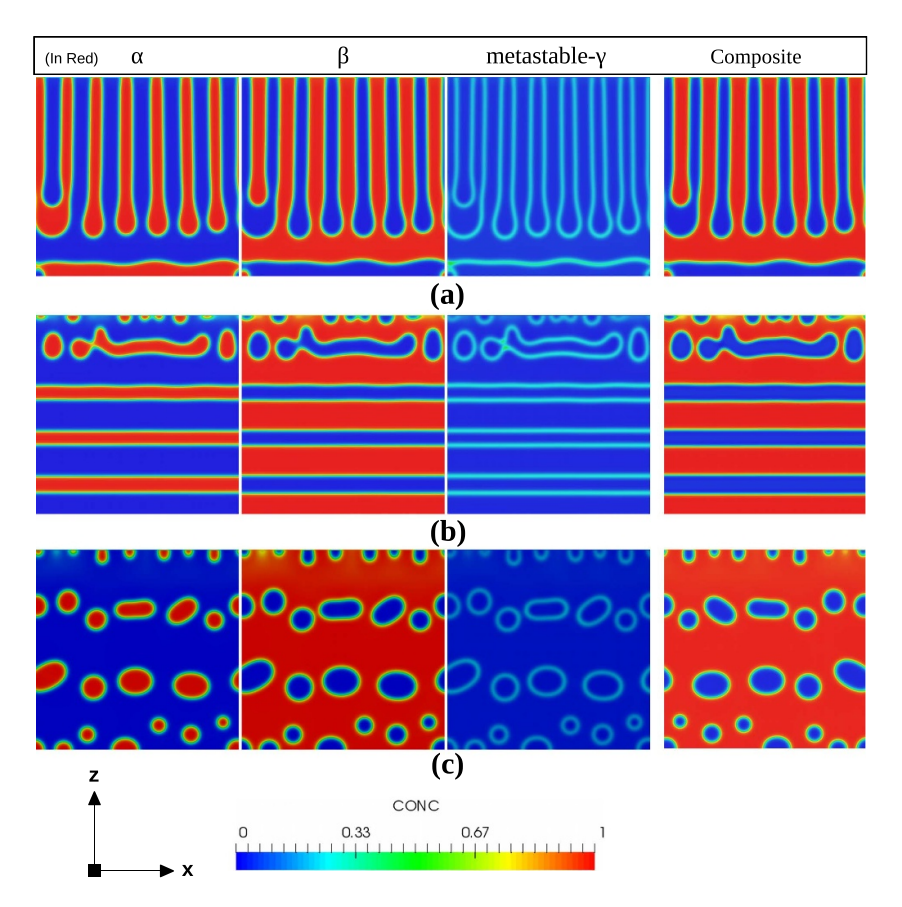


Figure 6. Morphological evolution of films at various compositions within the middle zone.(a) 40 *at.*%A, 50 *at.*%B, C resulting in binary lamellae (bL), (b) 30 *at.*%A, 60 *at.*%B, C resulting in pseudo-VCM, and (c) 20 *at.*%A, 70 *at.*%B, C resulting in core–shell (CS) morphology. Nanostructures show evolution of α , β and γ phases separately, as well as a composite.

When the film composition is changed to 30 at.%A, 60 at.%B, C, as indicated by label M in figure 2, bL gives way to a pV structure, which comprises horizontal bands of α in a β matrix. pV nanostructures, as seen in figure 6(b), resemble the VCMs that are typically observed in binary immiscible films [20–22] of equimolar compositions, with the distinction that the width of the minority phase bands are smaller than that of the majority phase. Similar to bLs, the metastable third phase, which is C-rich, forms at the interface between the α and β bands and was found to stabilize at all the tested deposition rates. Upon reducing the atomic ratio of A even further (20 at.%A, 70 at.%B, C, point N in figure 2), globules of the A-rich α phase form in a matrix of the majority β phase, while C forms a metastable phase at the interface, giving rise to a CS nanostructure. The CS nanostructures are observed to evolve at all deposition rates, within a small composition range around point N (see figure 2). Apparently, CS nanostructures are widely found in films of polymer blends [39–41] therefore, it is interesting

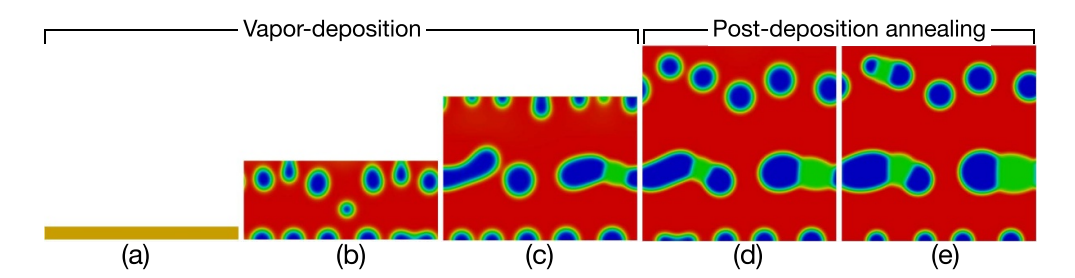


Figure 7. Morphological evolution of CS nanostructures during vapor-deposition and post-deposition annealing. Snapshots correspond to non-dimensional times (a) 10 (b) 100 (c) 200 (d) 290 (e) 500.

to isolate the small compositional window within which it can evolve in metallic systems, as well. During post-deposition annealing, the CS nanostructures have a strong tendency to coalesce as seen in figure 7.

4. Morphology maps

Constructing morphology maps, which involves correlating the zone boundaries with the resulting nanostructures, requires hundreds of simulation runs every time the processing conditions change. Therefore, the scope of the present study is limited to deposition rates (ν) of 0.31, 0.5, and 1.0. As shown in figure 8, the film compositions at which seven distinct nanostructured variants, one of which is hybrid (G-L), are mapped. Nanostructures with no periodic self-arrangement are labeled as random (R). We note that alloy composition along with the two kinetic factors, phase separation (M) and deposition rates (ν), determine the film nanostructure. Ternary lamellar (tL) morphology, shown yellow in figures 8(a) and (b), dominates the inner zone at lower $\nu \leqslant 0.5$, while vertically aligned beads and random non-assembled nanostructures form at larger ν . The bead morphology and hybrid G-L variants, shown in figure 8 in shades of blue and red, dominate the middle zone, accounting for nearly all of the nanoscale structures that evolve within this region. Additionally, the globular (G) morphology also appears at the extremities of this zone at a smaller $\nu = 0.31$. However, when ν is increased to 1.0, we note that the G-L hybrid nanostructures evolve in the regions originally occupied by globular nanostructures (G). This transition is one of the two notable ν -dependent transitions that occur across zones, and in this case, across the middle and outer zones. Noticeably, the other transitions appear at the boundary between the inner and middle zones. As the deposition rate increases, simulated films in the vicinity of 33 at.% A, 33 at.% B, C evolve as random non-assembled nanostructures (R). This transition happens in conjunction with the proliferation of the bead morphology into the inner zone at a composition of 30 at.% A, 30 at.% B, C. The outer zone morphologies are mostly unaffected by the deposition rate, with the binary lamellar (bL) (lavender), pV (purple), and CS (yellow) forming within their respective narrow composition ranges at all values of ν , except the globular (sky-blue) nanostructures, which also appear in the middle zone at low ν (figure 8(c)).

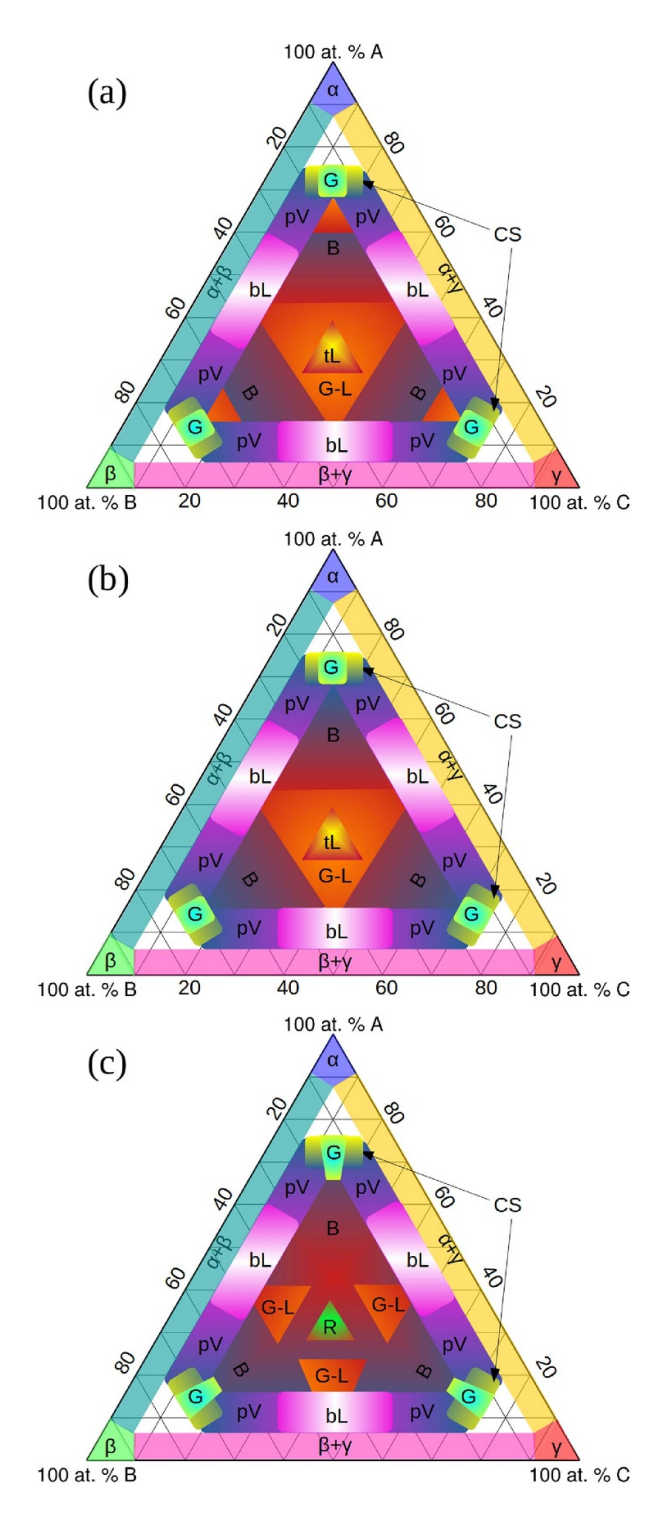


Figure 8. Ternary morphology maps plotted at distinct deposition rates, (a) ν = 0.31, (b) ν = 0.5, and (c) ν = 1.0.

5. Conclusion

In summary, we developed a phase-field model to simulate nanostructural evolution in vapordeposited ternary phase separating alloy films. Numerical simulations yielded a rich variety of nanoscaled film morphologies across a wide range of compositions and deposition rates. These nanostructured films were classified based on the morphology of the different phaseseparated domains which were found to be sensitive to alloy composition and the deposition rate. Dividing the compositional space into inner, middle, and outer allowed us to correlate it to the nanostructural morphology which is the highlight of our work. At equimolar compositions, the film nanostructure evolved into a ternary lamellar morphology at low deposition rates of 0.31, which transformed into a random nanostructure with no apparent self-assembly at rates higher than 1.0. With a slight alteration in film composition (30 at.%A, 30 at.%B, C), vertically aligned beaded nanostructures formed at an intermittent deposition rate of 0.5, while the lamellar and the random nanostructures continued to form at low and high deposition rates, respectively. For middle zone compositions, vertically aligned beads dominated, while a mixed lamellar-globular morphology appeared to form when the atomic ratio of one of the elements was lower than the other two. When the composition was adjusted such that two of the components were less than 15 at.%, globular nanostructured evolved. Within the outer zone, binary lamellar and pV morphologies were primarily observed. A CS nanostructure, which is more commonly observed in polymer blends, was also found to evolve. A low atomic ratio of C in the alloy prevented the formation of a γ -phase, leading to the formation of a metastable phase at the α/β interface in all the above three variants.

Morphology maps revealed that while deposition rate governs the nanostructural evolution at inner zone compositions, the impact of composition on nanostructuring is more pronounced in the middle and outer zones. These maps can potentially be used as guidance in the design of metamaterial films, however, since the reported study leverages a generic model with model parameters, the input parameters may need to be re-calibrated to the actual material and deposition condition. As a good starting point, the morphology maps reported in this work can be used to control the physical vapor-deposited Cu-Mo-Ag film nanostructures, known to be sensitive to the deposition rate and temperature [42]. Beyond alloy films, the above-reported phase-field approach can also be reformulated to simulate the nanostructural evolution in vertically aligned nanocomposite films of ZnO-Au, ZnO-Cu, and ZnO – Au_xAg_{1-x}, for use as hyperbolic metamaterials [43]. The present phase-field approach assumes the deposition flux to be occurring in discrete steps which are realized via the periodic addition of noisy layers. However, this can be substituted with a continuous deposition flux that would more closely resemble an actual PVD experiment.

Another interesting avenue worth exploring is the mechanisms by which nanostructural transitions occur in vapor-deposited ternary films. In our former work that focused on binary alloy films [21, 22], we deduced the mechanism of nanostructural transitions to be the minimization of total nanostructure interfacial energy. However, this criterion may have to be re-examined since ternary films entail three distinct interfaces $(\alpha/\beta, \beta/\gamma, \text{and } \gamma/\alpha)$ as opposed to one (α/β) in binary films. Previous simulations of nanostructural evolution in elastically homogenous binary immiscible films have shown that a large eigenstrain associated with the elastic misfit energy, slows down the kinetics of phase separation, causing a net increase in deposition rates at which distinct nanostructures can self-assemble. On the contrary, elastic inhomogeneity can selectively penalize the formation of interfaces during phase separation depending on the anisotropy of elastic modulus, especially at low deposition rates [44]. However, the role of misfit strains in the context of ternary films was not considered, which is worth analyzing [32, 37, 44]. Finally, the film surface in the present study was assumed to be flat to

limit the influence of surface irregularities on nanostructural evolution. However, the physics of hillock formation can be introduced to more closely resemble the film topology that is seen in experiments, by accounting for an additional vapor phase [45, 46].

Data availability statement

The data that support the findings of this study are available upon reasonable request from the authors.

Acknowledgments

KA acknowledges funding from the National Science Foundation (NSF) under Grant Nos. CMMI- 1763128 and CAREER-2145812.

ORCID iDs

```
Peichen Wu https://orcid.org/0000-0001-8788-6681
Kumar Ankit https://orcid.org/0000-0001-5283-5139
```

References

- [1] Vineis C J, Shakouri A, Majumdar A and Kanatzidis M G 2010 Adv. Mater. 22 3970-80
- [2] Heremans J P, Thrush C M and Morelli D T 2004 Phys. Rev. B 70 115334
- [3] Nötzel R 1996 Semicond. Sci. Technol. 11 1365
- [4] Kang H, Kee S, Yu K, Lee J, Kim G, Kim J, Kim J R, Kong J and Lee K 2015 Adv. Mater. 27 1408–13
- [5] Cai W, Chettiar U K, Kildishev A V and Shalaev V M 2007 Nat. Photon. 1 224-7
- [6] Nagpal P, Lindquist N C, Oh S H and Norris D J 2009 Science 325 594-7
- [7] Pendry J B 2000 Phys. Rev. Lett. 85 3966–9
- [8] Liu N, Guo H, Fu L, Kaiser S, Schweizer H and Giessen H 2008 Nat. Mater. 7 31-37
- [9] Chen G, Wang T and Stringfellow G 1990 Appl. Phys. Lett. 56 1–4
- [10] Norman A G, Seong T Y, Ferguson I T, Booker G R and Joyce B A 1993 Semicond. Sci. Technol.
- [11] Seong T, Norman A, Ferguson I and Booker G 1993 J. Appl. Phys. 73 8227–36
- [12] Ahrenkiel S P, Xin S H, Reimer P M, Berry J J, Luo H, Short S, Bode M, Al-Jassim M, Buschert J R and Furdyna J K 1995 Phys. Rev. Lett. 75 1586–9
- [13] Chen C Q, Pei Y T, Shaha K P and De Hosson J T M 2010 Appl. Phys. Lett. 96 073103
- [14] Peiro F, Cornet A, Morante J R, Georgakilas A, Wood C and Christou A 1995 Appl. Phys. Lett. 66 2391
- [15] Jun S W, Seong T Y, Lee J H and Lee B 1996 Appl. Phys. Lett. 68 3443-5
- [16] Fink V, Chevalier E, Pitts O J, Dvorak M W, Kavanagh K L, Bolognesi C R, Watkins S P, Hummel S and Moll N 2001 Appl. Phys. Lett. 79 2384–6
- [17] Francoeur S, Hanna M, Norman A and Mascarenhas A 2002 Appl. Phys. Lett. 80 243-5
- [18] Seppänen T, Persson P O Å, Hultman L, Birch J and Radnóczi G Z 2005 J. Appl. Phys. 97 083503
- [19] Bortoleto J R, Gutiérrez H R, Cotta M A and Bettini J 2005 Appl. Phys. Lett. 87 1-4
- [20] Lu Y, Wang C, Gao Y, Shi R, Liu X and Wang Y 2012 Phys. Rev. Lett. 109 1–5
- [21] Ankit K, Derby B, Raghavan R, Misra A and Demkowicz M J 2019 J. Appl. Phys. 126 075306
- [22] Raghavan R, Mukherjee A and Ankit K 2020 J. Appl. Phys. 128 175303
- [23] Fukutani K, Ishida Y, Tanji K and Den T 2007 Thin Solid Films 515 4629-35
- [24] Fukutani K, Tanji K, Saito T and Den T 2008 *Jpn. J. Appl. Phys.* 47 1140–6
- [25] Findik F 2002 Can. Metall. Q. 41 337-47
- [26] Hanna J A, Baker I, Wittmann M W and Munroe P R 2005 J. Mater. Res. 20 791-5

- [27] Liu T F and Wan C M 1985 Scr. Metall. 19 727-32
- [28] Löffler J F 2003 Intermetallics 11 529-40
- [29] Chang H J, Yook W, Park E S, Kyeong J S and Kim D H 2010 Acta Mater. 58 2483-91
- [30] Liu J M, Wu W H, Zhai W and Wei B 2019 Ultrason. Sonochem. 54 281-9
- [31] Chen L Q 1994 Acta Metall. Mater. 42 3503-13
- [32] Bhattacharyya S and Abinandanan T A 2003 Bull. Mater. Sci. 26 193-7
- [33] Cahn J W and Hilliard J E 1958 J. Chem. Phys. 28 258-67
- [34] Morral J E and Cahn J W 1971 Acta Metall. 19 1037-45
- [35] Kramer E J, Green P and Palmstrøm C J 1984 Polymer 25 473-80
- [36] Huang C, de La Cruz M O and Swift B 1995 Macromolecules 28 7996-8005
- [37] Sugathan S and Bhattacharya S 2020 Comput. Mater. Sci. 172 109284
- [38] Cogswell D A 2010 A phase-field study of ternary multiphase microstructures *PhD Thesis*Massachusetts Institute of Technology
- [39] del Campo A, de León A, Rodríguez-Hernández J and Mu noz-Bonilla A 2017 Langmuir 33 2872-7
- [40] Sprenger M, Walheim S, Budkowski A and Steiner U 2003 Interface Sci. 11 225-35
- [41] Walheim S, Ramstein M and Steiner U 1999 Langmuir 15 4828–36
- [42] Powers M, Derby B, Raeker E, Champion N and Misra A 2020 Thin Solid Films 693 137692
- [43] Paldi R, Lu J, Pachaury Y, He Z, Bhatt N, Zhang X, El-Azab A, Siddiqui A and Wang H 2022 Molecules 27 1785
- [44] Raghavan R, Farmer W, Mushongera L T and Ankit K 2021 Comput. Mater. Sci. 199 110724
- [45] Raghavan R, Chen P E, Jiao Y and Ankit K 2021 J. Appl. Phys. 129 245301
- [46] Chen P E, Raghavan R, Zheng Y, Li H, Ankit K and Jiao Y 2022 Phys. Rev. E 105 025306